



Keck adaptive optics images of Jupiter's north polar cap and Northern Red Oval

Imke de Pater^{a,b,c,*}, Michael H. Wong^a, Katherine de Kleer^a, Heidi B. Hammel^{d,e}, Máté Ádámkóvics^a, Al Conrad^{f,g}

^aAstronomy Department, 601 Campbell Hall, University of California, Berkeley, CA 94720, USA

^bDelft Institute of Earth Observation and Space Systems, Delft University of Technology, NL-2629 HS Delft, The Netherlands

^cSRON Netherlands Institute for Space Research, 3584 CA Utrecht, The Netherlands

^dAssociation of Universities for Research in Astronomy, 1212 New York Avenue NW, Suite 450, Washington, DC 20005, USA

^eSpace Science Institute, 4750 Walnut Avenue, Suite 205, Boulder, CO 80301, USA

^fW.M. Keck Observatory, Waimea, HI 96743, USA

^gMax-Planck-Institut fuer Astronomie Koenigstuhl 17, D-69117 Heidelberg, Germany

ARTICLE INFO

Article history:

Received 17 December 2010

Revised 28 February 2011

Accepted 4 March 2011

Available online 21 March 2011

Keywords:

Jupiter, Atmosphere
Infrared observations
Adaptive optics

ABSTRACT

We present observations at near-infrared wavelengths (1–5 μm) of Jupiter's north polar region and Northern Red Oval (NN-LRS-1). The observations were taken with the near-infrared camera NIRC2 coupled to the adaptive optics system on the 10-m W.M. Keck Telescope on UT 21 August 2010. At 5- μm Jupiter's disk reveals considerable structure, including small bright rings which appear to surround all small vortices. It is striking, though, that no such ring is seen around the Northern Red Oval. In de Pater et al. [2010a. *Icarus* 210, 742–762], we showed that such rings also exist around all small vortices in Jupiter's southern hemisphere, and are absent around the Great Red Spot and Red Oval BA. We show here that the vertical structure and extent of the Northern Red Oval is very similar to that of Jupiter's Red Oval BA. These new observations of the Northern Red Oval, therefore, support the idea of a dichotomy between small and large anticyclones, in which ovals larger than about two Rossby deformation radii do not have 5- μm bright rings. In de Pater et al. [2010a. *Icarus* 210, 742–762], we explained this difference in terms of the secondary circulations within the vortices. We further compare the brightness distribution of our new 5- μm images with previously published radio observations of Jupiter, highlighting the depletion of NH_3 gas over areas that are bright at 5 μm .

© 2011 Elsevier Inc. All rights reserved.

1. Introduction

The planet Jupiter is covered by numerous ovals, varying in size from tiny, barely distinguishable spots to large vortices like the Great Red Spot (GRS) and Red Oval BA. At short (~ 0.2 – $2.5 \mu\text{m}$) wavelengths, where Jupiter is seen in reflected sunlight, the ovals are either dark or bright compared to the background atmosphere. Most of the tiny ovals are at high latitudes ($\gtrsim |50|^\circ$), and are easiest to spot at a wavelength of 5 μm , where they show up as small infrared-bright rings. This emission is thermal emission, typically arising from depths $\gtrsim 4$ bar in Jupiter's atmosphere. These rings tightly surround the visible ovals, and coincide with the visibly bluish-grey rings around the ovals (de Pater et al., 2010a; hereafter referred to as Paper 1). In Paper 1 we presented observations and theoretical calculations on the vertical structure of and secondary circulation in jovian vortices. Observationally, we constrained the maximum radius of these rings to be less than twice the local Rossby deformation radius, L_R . The GRS and Oval BA—which have radii

larger than $2L_R$ —do not have 5- μm bright rings, and now we show that the Northern Red Oval also adheres to this rule. Although 5- μm emission is commonly observed around the GRS and Red Oval BA, we show in Paper 1 that this emission is well outside the dynamical boundaries of the large anticyclones, and the incomplete/patchy appearance of the 5- μm emission is distinctly different from the coherent rings seen around small anticyclones.

In this paper we present observations of Jupiter's northern hemisphere and the Northern Red Oval at a latitude $\sim 42^\circ\text{N}$. Rogers et al. (2010) summarized observations of this spot as taken by amateur astronomers over the past ~ 15 years: The Northern Red Oval, referred to as NN-LRS-1 (Little Red Spot 1 in Jupiter's North North Temperate Zone – NNTZ), has been observed in the past going back as far as 1993. Since that time it has varied in color from off-white to reddish, and the spot is always bright at wavelengths of strong methane absorptions (e.g., 889 nm). During the summer of 2010, the Northern Oval was red. Our observations of this feature provide further evidence of the dichotomy in the thermal infrared appearances of small and large ovals. In Paper 1, we explained this difference in terms of the secondary circulations of the vortices, in which air baroclinically rises along the central axis of an anticyclone and diverges at the top. What goes up must come

* Corresponding author at: Astronomy Department, 601 Campbell Hall, University of California, Berkeley, CA 94720, USA. Fax: +1 510 642 3411.

E-mail address: imke@berkeley.edu (I. de Pater).

down, and the return flow descends at a distance equal to the smaller of (1) $2L_R$ or (2) the outer radius of the vortex.

2. Observations and data reduction

We observed Jupiter with the 10-m W.M. Keck II telescope on Mauna Kea, Hawaii, on UT 21 August 2010. Jupiter's heliocentric and geocentric distances were $r = 4.961$ AU and $\Delta = 4.088$ AU, respectively. We used NIRC2, a near-infrared camera with a 1024×1024 Aladdin-3 InSb array, coupled to the adaptive optics (AO) system. We utilized the wide-field camera, covering a field $\sim 40'' \times 40''$ at a plate scale of 39.69 mas/pixel, for observations at 1–2.5 μm (see Table 1 for filter specifics). At 5 μm the sky background saturates the wide-field camera, so we used the narrow-field camera. The narrow-field camera covers a field $\sim 10'' \times 10''$ at 9.94 mas/pixel. Since Jupiter is too large to be used for wavefront sensing, we use Callisto as a tipilt “star” when it was close enough to Jupiter (see Paper 1 for details on such observations).

All images were processed using standard near-infrared data reduction techniques: flat-fielded, sky-subtracted, corrected for the geometric distortion, and bad pixels replaced by the median of surrounding pixels (see Paper 1 for details). The absolute calibration of the images is based on observations of the IR standard star HD1160 (Elias et al., 1982), and the final photometry on Jupiter was “tweaked”¹ using the IRTF spectrum from Rayner et al. (2009), as well as previously published observations of Jupiter (see de Pater et al., 2010a.). We estimate our final flux calibration to be accurate to $\lesssim 15\text{--}20\%$.

To compare images where Jupiter is observed in reflected sunlight (1.1–2.5 μm) with previous results and with physical models, we converted the observed flux densities to the dimensionless parameter I/F , where I is the reflected intensity and πF the solar flux density at Jupiter's distance (e.g., Paper 1 and Hammel et al., 1989). The units on the 5- μm images were converted to brightness temperature per pixel, using Planck's equation and the assumption of a blackbody radiator. From features on Jupiter that appear to be unresolved we determined a typical resolution on Jupiter of $\sim 0.12\text{--}0.16''$ ($\sim 360\text{--}480$ km) in the full-disk (1.2–2.5 μm) images, and $0.08\text{--}0.10''$ at 5 μm ($\sim 240\text{--}300$ km).

Since Jupiter rotates, features on the planet will shift from image to image, even if taken only minutes apart (by $\sim 0.25''/\text{min}$ at the sub-Earth point). This complicates mosaicing the small field of view 5- μm images. To successfully combine our 43 individual frames taken over a span of 105 min, we used a three-step process. In the first step, we navigated those frames containing a portion of Jupiter's limb by roughly aligning a coordinate grid to the portion of the limb visible in each image. This first step is complicated by variability in Jupiter's apparent radius depending on the 5- μm radiance. Then we identified atmospheric features visible in multiple frames, and applied a least-squares minimization to ensure that the features were located at the same latitude and longitude in all common frames. Three to five features per frame were identified at different latitudes to reduce errors caused by zonal drift rates. Finally, images with no visible limb were navigated by linking tie-points to frames where the limb was visible, using the tie-nav procedure described in Lii et al. (2010).

3. Results and discussion

Selected full-disk images of Jupiter are shown in Fig. 1. Observations at 1.58 μm show Jupiter's cloud layers, while higher altitude haze is most prominent at the methane-absorbing wavelengths

Table 1
Filter specifics and I_0/F^a for the three large ovals.

Filter name	Wavelength (μm)	$\Delta\lambda$ (μm)	I_0/F^a GRS	I_0/F^a Oval BA	I_0/F^a N. Red Oval
Jcont	1.2132	0.0198	0.382	0.287	0.318
Pabeta	1.2903	0.0193	0.605	0.543	0.519
Hcont	1.5804	0.0232	0.658	0.596	0.551
Fell	1.6455	0.0256	0.074	0.040	0.049
H ₂ ($v = 1\text{--}0$)	2.1281	0.0342	0.034	0.014	0.021
Ms	4.67	0.24			

^a I_0/F : The observed I/F has been corrected for viewing angle and illumination effects using a Minnaert coefficient $k = 0.9$ (see Eq. (2) and details in Paper 1). The I/F values were determined from the observations by taking the median value in a box at the center of the various ovals: a $3^\circ \times 3^\circ$ square box for the GRS; a $0.6^\circ \times 0.6^\circ$ box for Oval BA, and a $2^\circ \times 2^\circ$ box for the Northern Red Oval. We note, though, that the I/F values do not depend much on the size of the box. Typical uncertainties in the final I_0/F values my range up to 10–20%.

1.65 and 2.13 μm . Fig. 2 shows a mosaic of 5 μm images, where bright regions signify areas that are cloud-free down to at least the ~ 4 -bar level, and perhaps down to $\sim 5\text{--}7$ bar, i.e., well within the water cloud (Paper 1). The north polar cap is completely filled with 5- μm bright areas, many in the form of bright rings. These rings typically surround the small ovals that are seen in reflected sunlight, which is best shown in the color composites in Fig. 3. Most striking is the lone Northern Red Oval at 42°N in Fig. 3b (white in Fig. 3a; blue in Fig. 3b). Despite being surrounded by a relatively dark ‘ring’ in Fig. 3a, no 5- μm emission is seen in Fig. 3b. This intriguing anomaly is discussed in more detail in the following subsections.

Figs. 2 and 3 further show the large cyclonic regions on Jupiter (e.g., to the north and south-east of the Northern Red Oval) in exquisite detail. Thermal emission from Jupiter's deep ($P > 4$ bar) atmosphere is leaking through ‘holes’ or ‘rifts’ in the clouds, giving the regions a filamentary structure. In addition, although enhanced 5- μm emission in the North Equatorial Belt (NEB) was already reported in the sixties (Westphal, 1969), the data presented in Figs. 2 and 3 reveal fine details in this belt that have not been imaged before at this resolution. Interesting features, for example, are the 5- μm bright swirls around the small ovals at 15°N , which reveal 5- μm bright dots at their center. We also note the narrow band of 5- μm ‘specks’ at $22\text{--}23^\circ\text{N}$, coinciding with the nodules in the orange band in Fig. 3a.

In Paper 1 we determined that depths of at least 4 bar, and perhaps 5–7 bar, are probed in these 5- μm bright areas. Our analysis in that paper was based on the work by Roos-Serote et al. (1999), who presented fits to Voyager IRIS spectra of 5- μm hot spots. Using radio observations, Sault et al. (2004) show that large 5- μm bright spots are not only free of clouds, but the air is also “dry” over a similar pressure range. The latter authors show that the ammonia abundance in such hot spots is $\sim 3 \times 10^{-5}$ (i.e., ~ 4 times less than the solar value) down to at least the 4 bar pressure level. The globally-averaged NH_3 abundance in the North Equatorial Belt (NEB) is $\sim 6 \times 10^{-5}$ down to the 5–6 bar level, which itself is a factor of 2 less than the NH_3 abundance in the Equatorial zone (EZ) (e.g., de Pater et al., 2001). The difference in the NH_3 abundance between the EZ and NEB is consistent with greater 5- μm emission in the NEB than the EZ. A low ammonia abundance ($\sim 60\%$ of the NH_3 abundance in the EZ) has also been reported in Jupiter's polar regions (de Pater, 1986). This low NH_3 abundance again coincides with the dense coverage of 5- μm bright regions over Jupiter's pole, as discussed above. We encourage dynamicists to use the detailed morphology of the 5- μm emissions to infer and model the detailed dynamics in Jupiter's atmosphere. In particular, we think that such models may help explain how ammonia gas can be globally depleted at pressure levels of ~ 0.6 down to 4–6 bar by factors of order 5–10 relative to the deep

¹ We decreased Jupiter's intensity by 10% at 1.29 μm , and increased it by 15% at 2.13 μm .

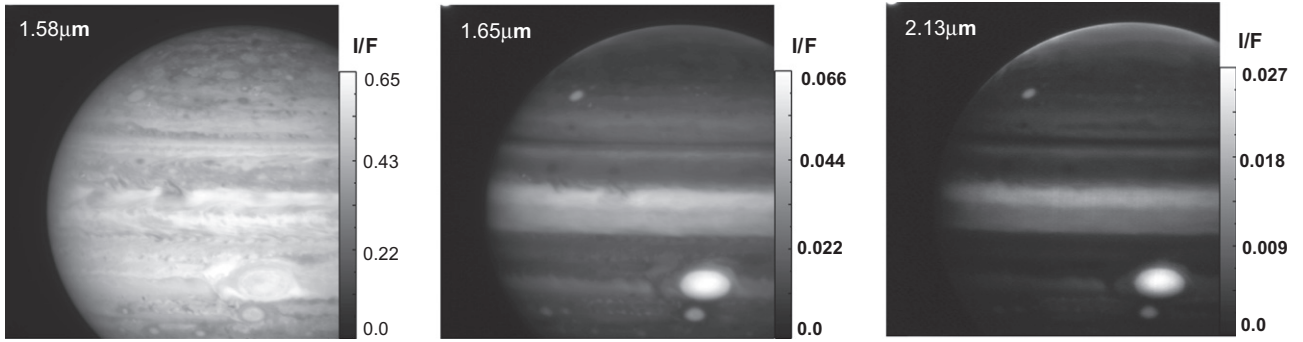


Fig. 1. Full disk images at 1.58, 1.65, and 2.13 μm , taken with the Keck AO system on UT 21 August 2010. The Northern Red Oval is bright against the background at 1.65 and 2.13 μm . Both the GRS and Red Oval BA are visible in the southern hemisphere. The (linear) intensity scale in each image is stretched so the contrast is optimal; the I/F scale is shown on the right of each image.

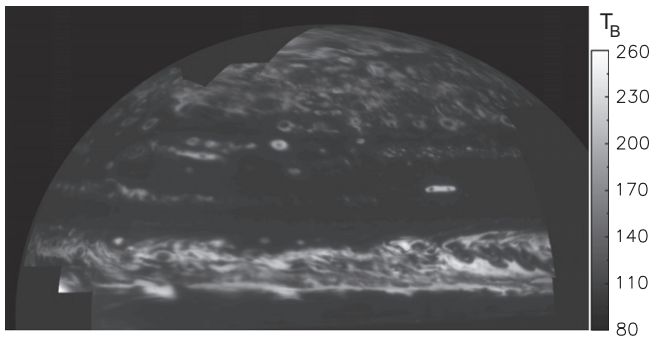


Fig. 2. Mosaiced view of Jupiter's northern hemisphere at 5 μm . Typical brightness temperatures, T_B , are 230–240 K near the northern polar cap, and 250–260 K in the NEB.

mixing ratio of $6.6 \pm 2.5 \times 10^{-4}$ (Wong et al., 2004), as the simplest models for convection in Jupiter's interior suggest that condensable vapors should be well-mixed up to the condensation level (de Pater et al., 2001; Showman and de Pater, 2005).

3.1. Vertical structure of the large ovals

We constrained the vertical structure of the three large ovals – the GRS, Oval BA and the Northern Red Oval – in the same way as in Paper 1. Our radiative transfer (RT) program, along with its simplifications, limitations and potential degeneracies (e.g., between particle size and density) was discussed in detail in Paper 1. In that paper we also show contribution functions and fits to the disk-averaged spectrum of Rayner et al. (2009) (see also de Pater et al., 2010b). Our results for the three large ovals are summarized in Fig. 4. As shown, the vertical structure of these three ovals is very similar to one another, and to our findings in Paper 1. The main difference with Paper 1 is that for all three ovals, best matches to the 2010 data were obtained by splitting the upper haze layer from Paper 1 into two layers: one at pressures $2 < P < 110$ mbar, and one at $110 < P < 200$ mbar.

In Paper 1 we pointed out that the density of the haze layers in the upper troposphere and lower stratosphere (at pressures $2 \text{ mbar} < P < 650 \text{ mbar}$) is typically 5–8 times higher for Oval BA, the GRS, and the small red Oval 2, than for the smaller white Ovals 5 and 6. The Northern Red Oval similarly shows a high density in the upper troposphere. Our modeling efforts thus support our main conclusions in Paper 1: the difference between the white and red ovals is primarily caused by a difference in the density of the tropospheric haze above ($P < 650$ mbar).

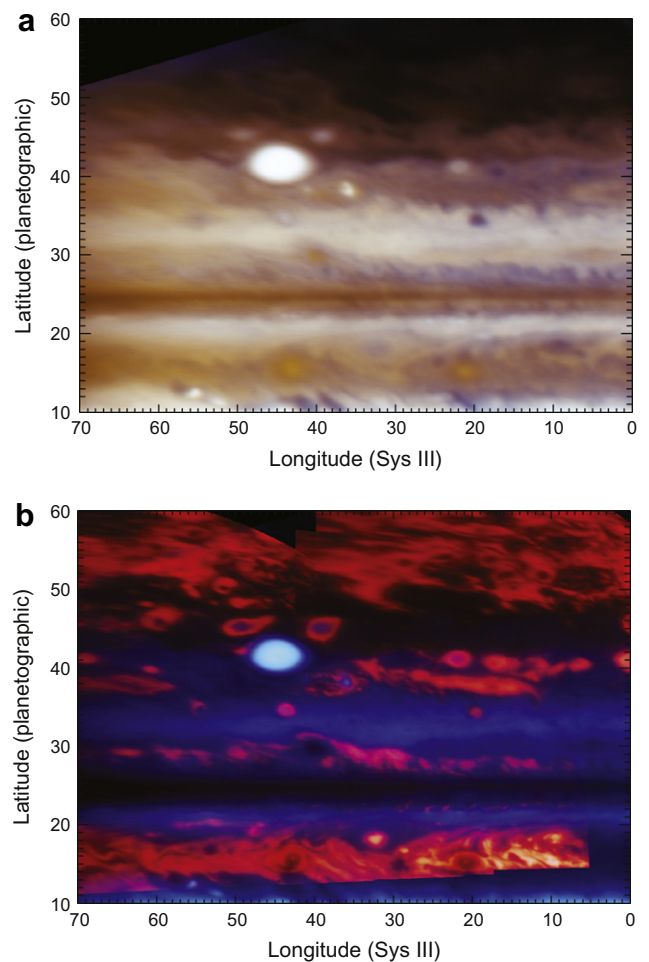


Fig. 3. (a) Deprojected map of Jupiter's Northern Red Oval. Images at 1.29 (green), 1.58 (red), and 1.65 (blue) μm were combined to create this 3-color composite. The oval shows up bright white in this view, at a planetographic latitude of 42°N and System III West longitude of 45° . (b) Deprojected 2-color composite map of Jupiter's Northern Red Oval. Images at 1.65 (blue) and 5 (red) μm were combined. The oval, visible at 1.65 μm , is not surrounded by a 5- μm bright ring, in contrast to the smaller ovals, which all show such rings around their periphery.

3.2. Morphology of the Northern Red Oval

The east–west radius of the Northern Red Oval is 2990 km, as determined by the width at half-maximum of the 1.65- μm reflectivity (Fig. 1). This is essentially the same radius as determined for Oval BA from HST data taken in 2006 (Asay-Davis et al., 2009). In

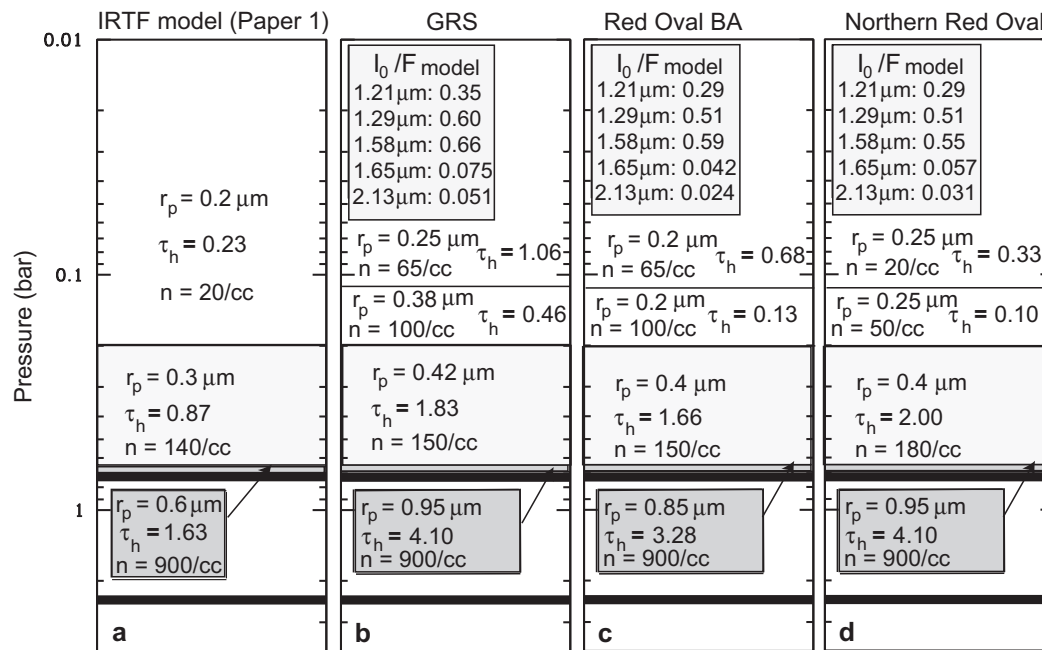


Fig. 4. (a) Model from Paper 1 that matches Rayner et al.'s (2009) disk-averaged IRTF spectrum. The particle number density is indicated by n , τ_h is the geometric optical depth (Eq. (3) in Paper 1), and r_p the particle radius in μm . The upper (stratospheric) haze layer in this model is similar to that above the small anticyclonic white ovals (Ovals 5 and 6 in Paper 1). (b–d) Sketch of parameters that agree with the I_0/F measurements (Table 1) of the GRS, Oval BA and the Northern Red Oval, respectively. The modeled values are indicated in the box at the top for each oval. We list the I_0/F values, i.e., we “corrected” the modeled I/F values in the same way as the observed I/F s using a Minnaert coefficient $k = 0.9$ (see Table 1). In all panels, the stratospheric haze extends up to 2 mbar. The thick black bars near 0.75 and 2.5 bar represent the NH_3 -ice and NH_4SH clouds.

the latter paper, the authors define the radius of a vortex by its velocity field rather than its cloud morphology, as this is more meaningful in a physical sense. Wong et al. (2011) show that for the largest vortices, the size and shape of the area of enhanced tropospheric haze, e.g., that seen at $1.65 \mu\text{m}$, is nearly coincident with the dynamical boundary defined by the ring of maximum azimuthal velocity. The radius of the Northern Red Oval as determined by the visible clouds/hazes is larger, $\sim 3750 \text{ km}$.

At the planetographic latitude of the Northern Red Oval ($\theta = 42^\circ\text{N}$), the Rossby deformation radius $L_R \approx 1380 \text{ km}$ (assuming that $L_R \sim 2300 \text{ km}$ at $\theta \sim 23^\circ\text{S}$, and that it scales with latitude as $1/|\sin \theta|$, Shetty and Marcus, 2010). The Northern Red Oval therefore has a radius of $2.2L_R$ (the radius of the visible oval is $\sim 2.7L_R$), while the other vortices in Figs. 1–3 have radii $< 2L_R$. These smaller vortices are surrounded by $5\text{-}\mu\text{m}$ bright rings. Our observations reinforce the dichotomy that we described based on southern hemispheric observations in Paper 1: that anticyclones have $5\text{-}\mu\text{m}$ bright rings when their characteristic radius is $< 2L_R$.

3.3. Secondary circulation

In Paper 1 we developed a model of the secondary circulation for vortices in a subadiabatic atmosphere. We show that air is baroclinically rising at the center of such a vortex, and while the parcel is rising air cools adiabatically, and it “dries out” as condensable gases form clouds. In a subadiabatic atmosphere this leads to the top of the vortex being colder than the ambient temperature at the same pressure level. This is exactly what is observed for several ovals at mid-infrared wavelengths (e.g., Conrath et al., 1981; Cheng et al., 2008; Fletcher et al., 2010). In a stable long-lived vortex, gas that is rising upwards, must fall back down. Thus when the gas reaches the upper boundary of the vortex, it spreads radially. In Paper 1 we postulate that the gas descends at the location of the $5\text{-}\mu\text{m}$ bright rings, as such rings are indicative of dry subsiding air. A typical distance for gas to move radially away from the center of the vortex is the Rossby deformation radius, L_R , which is the

characteristic length scale over which the effects of the Coriolis force are balanced by the buoyancy forces in a geostrophic flow (c.f. Pedlosky, 1987). In Paper 1 we show observationally that the radius of such $5\text{-}\mu\text{m}$ bright rings in the southern hemisphere never exceeds $2L_R$. Figs. 1–3 show that the same holds true in the north.

In an analysis of the 2010 fading of the South Equatorial Belt (SEB), Fletcher et al. (2011) present observations at 8.6 and $10.8 \mu\text{m}$ which reveal that the top of the Northern Red Oval is slightly colder than the ambient temperature at the same pressure level, similar to findings for the GRS and Oval BA (e.g., Conrath et al., 1981; Cheng et al., 2008; Fletcher et al., 2010). This suggests that air is baroclinically rising along the center axis of the oval. Fletcher et al. (2011) further noticed that the lower-than-ambient temperature above the Northern Red Oval extends over an area that is smaller than that covered by the aerosols. This implies that the subsiding part of the secondary circulation probably does take place inside the oval; the temperature is only below-ambient at the top of the vortex where air is rising, not subsiding. One may ask the question: why is the Northern Oval's red color not confined to an annulus as in Oval BA? Moreover, the color appears to vary from red to off-white over time. In Paper 1 we favored West et al.'s (1986) “hiding” and “exposing” mechanism to explain an oval's red color. In this model, red chromophores act as condensation nuclei. If the temperature is below the condensation temperature of ammonia, NH_3 -gas condenses onto these chromophores, “hiding” the original particulates. When the temperature rises above this level, the ice will sublime and “expose” the original chromophore. Based on this model, an oval's color may, in essence, be regarded as a “thermometer”. However, just as for the GRS, the red color can also be hidden from view by a white haze above it. Ideally, observations over a broad ($\sim 0.2\text{--}2.5 \mu\text{m}$) wavelength range should be taken both when the oval is red and when it is white, so that one can identify potential changes in the Northern Red Oval's vertical structure through RT calculations. Additional data at mid-infrared ($\sim 8\text{--}20 \mu\text{m}$) wavelengths will provide information on the oval's temperature and potential changes therein.

4. Conclusions

Near-infrared observations of Jupiter's Northern Red Oval, NN-LRS-1, show a striking similarity between this oval and the Red Oval BA. Both ovals have diameters over ~ 6000 km, have a red color, and a similar vertical structure. Most striking is the absence of $5\text{-}\mu\text{m}$ bright rings around their periphery, as such rings are seen around all smaller ovals. This observation, together with Fletcher et al.'s (2011) results at 8.6 and $10.8\ \mu\text{m}$, can be explained in terms of the secondary circulation scheme for anticyclones that we presented in Paper 1:

- (i) Fletcher et al.'s observation that the top of the Northern Red Oval is colder than the ambient temperature suggests that air is baroclinically rising along the center of the vortex in a subadiabatic atmosphere.
- (ii) The absence of a $5\text{-}\mu\text{m}$ bright ring around the periphery of the Northern Red Oval, together with Fletcher et al.'s observation that the lower-than-ambient temperature extends over an area that is smaller than that covered by the aerosols, suggests that the return flow of the secondary circulation falls within the visible oval. This is consistent with our suggestion in Paper 1 that the finite horizontal length scale of the secondary circulation must be less than twice the Rossby deformation radius, $2L_R$.

Vortices with radii $>2L_R$ are rare on Jupiter. A $5\text{-}\mu\text{m}$ imaging time-series showing the growth of a vortex from $R < 2L_R$ to $R > 2L_R$ would be an ideal test of our finding that vortex morphology is regulated by size. Also, to get a better understanding of the Northern Oval's red color, observations should be taken over a broad ($\sim 0.2\text{--}2.5\ \mu\text{m}$ as well as in the mid-IR) wavelength range both at times that the oval is white and when it is red. Only through such observations combined with detailed RT calculations, can one show whether the vertical structure and temperature of the Northern Red Oval changes when its color changes. This, in turn, may provide information on the origin of any red color on Jupiter.

The brightness distribution of our new $5\text{-}\mu\text{m}$ images sheds a new light on radio maps of Jupiter's thermal emission, and the spatial distribution of the ammonia abundance derived from these maps. Areas that are bright at a wavelength of $5\ \mu\text{m}$ are characterized by a lower-than-average NH_3 abundance, indicative of subsiding motions of dry air. Although this comparison was made before for $5\text{-}\mu\text{m}$ hot spots (Sault et al., 2004), it was never revealed in Jupiter's polar regions. Detailed studies correlating images at these different wavelengths may help to better understand Jupiter's global dynamics and the overall depletion of NH_3 gas in Jupiter's troposphere at $0.6 < P < 4\text{--}6$ bar.

Acknowledgments

All data were obtained with the W.M. Keck Observatory, which is operated by the California Institute of Technology, the University

of California, and the National Aeronautics and Space Administration. The Observatory was made possible by the generous financial support of the W.M. Keck Foundation. We benefitted greatly from the use of JPL's Horizons system and SETI's Planetary Rings Node. The authors extend special thanks to those of Hawaiian ancestry on whose sacred mountain we are privileged to be guests. Without their generous hospitality, none of the observations presented would have been possible.

References

- Asay-Davis, X.S., Marcus, P.S., Wong, M.H., de Pater, I., 2009. Jupiter's evolving Great Red Spot: Velocity measurements with the advection corrected correlation image velocimetry automated cloud tracking method. *Icarus* 203, 164–188.
- Cheng, A.F. et al., 2008. Changing characteristics of Jupiter's Little Red Spot. *Astron. J.* 135, 2446–2452.
- Conrath, B.J., Flasar, F.M., Pirraglia, J.A., Gierasch, P.J., Hunt, G.E., 1981. Thermal structure and dynamics of the jovian atmosphere. 2. Visible cloud features. *J. Geophys. Res.* 86, 8769–8775.
- de Pater, I., 1986. Jupiter's zone-belt structure at radio wavelengths: II. Comparison of observations with model atmosphere calculations. *Icarus* 68, 344–365.
- de Pater, I., Dunn, D., Zahnle, K., Romani, P.N., 2001. Comparison of Galileo probe data with ground-based radio measurements. *Icarus* 149, 66–78.
- de Pater, I., Hammel, H., Fletcher, L., Orton, G., Pérez-Hoyos, S., Wong, M.H., Luszcz-Cook, S., Sánchez-Lavega, A., Boslough, M., 2010b. A multi-wavelength study of the 2009 impact on Jupiter: Comparison of high resolution images from Gemini, Keck and HST. *Icarus* 210, 722–741.
- de Pater, I., Wong, M.H., Marcus, P.S., Luszcz-Cook, S., Ádámkóvics, M., Conrad, A., Asay-Davis, X., Go, C., 2010a. Persistent rings in and around Jupiter's anticyclones – Observations and theory. *Icarus* 210, 742–762 (Paper 1).
- Elias, J.H., Frogel, J.A., Matthews, K., Neugebauer, G., 1982. Infrared standard stars. *Astron. J.* 87, 1029–1034.
- Fletcher, L.N. et al., 2010. Thermal structure and composition of Jupiter's Great Red Spot from high-resolution thermal imaging. *Icarus* 208, 306–328.
- Fletcher, L.N. et al., 2011. Jovian temperature and cloud variability during the 2009–2010 Fade of the South Equatorial Belt. *Icarus* 213, 564–580.
- Hammel, H.B., Baines, K.B., Bergstrahl, J.T., 1989. Vertical aerosol structure of Neptune: Constraints from center-to-limb profiles. *Icarus* 80, 416–438.
- Lii, P.S., Wong, M.H., de Pater, I., 2010. Temporal variation of the tropospheric cloud and haze in the jovian equatorial zone. *Icarus* 209, 591–601.
- Pedlosky, J., 1987. *Geophysical Fluid Dynamics*. Springer-Verlag, New York.
- Rayner, J.T., Cushing, M.C., Vacca, W.D., 2009. The IRTF spectral library: Cool stars. *Astrophys. J.* 185 (Suppl.), 289–432. <http://irtfweb.ifa.hawaii.edu/~spex/IRTF_Spectral_Library/>.
- Rogers, J.H., Adamoli, G., Mettig, H.-J., 2010. Jupiters high-latitude storms: A little red spot tracked through a jovian year. *J. Brit. Astronom. Assoc.* 121, 19–29.
- Roos-Serote, M., Drossart, P., Encrenaz, Th., Carlson, R.W., Leader, F., 1999. Constraints on the tropospheric cloud structure of Jupiter from spectroscopy in the $5\text{-}\mu\text{m}$ region: A comparison between Voyager/IRIS, Galileo-NIMS, and ISO-SWS spectra. *Icarus* 137, 315–340.
- Sault, R.J., Engel, C., de Pater, I., 2004. Longitude-resolved imaging of Jupiter at $\lambda = 2\ \text{cm}$. *Icarus* 168, 336–343.
- Shetty, S., Marcus, P.S., 2010. Changes in Jupiters Great Red Spot (1979–2006) and Oval BA (2000–2006). *Icarus* 210, 182–201.
- Showman, A.P., de Pater, I., 2005. Dynamical implications of Jupiter's tropospheric ammonia abundance. *Icarus* 174, 192–204.
- West, R.A., Strobel, D.F., Tomasko, M.G., 1986. Clouds, aerosols and photochemistry in the jovian atmosphere. *Icarus* 65, 161–217.
- Westphal, J.A., 1969. Observations of localized 5 micron radiation from Jupiter. *Astrophys. J.* 157, L63–L64.
- Wong, M.H., Mahaffy, P.R., Atreya, S.K., Niemann, H.B., Owen, T.C., 2004. Updated Galileo probe mass spectrometer measurements of carbon, oxygen, nitrogen, and sulfur on Jupiter. *Icarus* 171, 153–170.
- Wong, M.H., de Pater, I., Marcus, P.S., Asay-Davis, X., Go, C.Y., 2011. Vertical structure of Jupiter's Oval BA before and after it reddened: What changed? *Icarus*, submitted for publication.